Journal of
Synchrotron Radiation

ISSN 0909-0495

Received 2 February 2010
Accepted 9 March 2010

Performance of a four-element Si drift detector for X-ray absorption fine-structure spectroscopy: resolution, maximum count rate, and dead-time correction with incorporation into the *ATHENA* data analysis software

J. C. Woicik,[a]* B. Ravel,[a] D. A. Fischer[a] and W. J. Newburgh[b]

[a]National Institute of Standards and Technology, Gaithersburg, MD 20899, USA, and [b]National Synchrotron Light Source, Brookhaven National Laboratory, Upton, NY 11973, USA. E-mail: woicik@bnl.gov

The performance of a four-element Si drift detector for energy-dispersive fluorescence-yield X-ray absorption fine-structure measurements is reported, operating at the National Institute of Standards and Technology beamline X23A2 at the National Synchrotron Light Source. The detector can acquire X-ray absorption fine-structure spectra with a throughput exceeding 4×10^5 counts per second per detector element ($>1.6 \times 10^6$ total counts per second summed over all four channels). At this count rate the resolution at 6 keV is approximately 220 eV, which adequately resolves the Mn $K\alpha$ and $K\beta$ fluorescence lines. Accurate dead-time correction is demonstrated, and it has been incorporated into the *ATHENA* data analysis program. To maintain counting efficiency and high signal to background, it is suggested that the incoming count rate should not exceed ~70% of the maximum throughput.

Keywords: Si drift detector; X-ray absorption fine-structure spectroscopy; dead-time correction; *ATHENA* data analysis software.

1. Introduction

In 1984, Gatti & Rehak described a novel charge-transport scheme in semiconductors that led to the development of the silicon drift detector (SDD) (Gatti & Rehak, 1984). It is based on the full depletion of a silicon wafer by a virtual electrode. A secondary electric field is then used to transport charge. As Gatti & Rehak explained, it is the small charge-collecting capacitance of the device that has the advantage of shorter rise times and higher gains over other charge-collecting devices. For X-ray absorption fine-structure (XAFS) spectroscopy applications, this development translates to a detector that can operate at faster count rates and higher temperatures than standard silicon or germanium lithium drifted detectors (SiLi or GeLi). In addition, the capacitance of the SDD is independent of its active area, thereby affording the production of large area detectors without the loss of resolution suffered by SiLi and GeLi detectors. For these reasons the SDD has become an attractive solution for cost effective, high-resolution and high-count-rate energy-dispersive fluorescence-yield XAFS measurements (Strüder *et al.*, 1998; Welter *et al.*, 2009; Letard *et al.*, 2006), and this trend is likely to continue with the increasing flux afforded by the next-generation synchrotron sources.

In this work we demonstrate the energy resolution and high-count-rate performance of a newly commissioned commercially available four-element SDD operating at the National Institute of Standards and Technology (NIST) XAFS beamline X23A2 at the National Synchrotron Light Source (NSLS). In addition to characterizing the performance of the detector, we carefully studied and report on its dead-time and the corrections necessary to obtain accurate XAFS spectra in the high-count-rate limit. This dead-time correction has been incorporated into the *ATHENA* (Ravel & Newville, 2005) XAFS data analysis program that should facilitate use by the synchrotron community not only for the SDD but also for standard SiLi and GeLi detectors.

2. Experimental

The detector was procured from SII Nanotechnology[1]. It is composed of four circular SDD elements, each with an active area of approximately 50 mm^2. The detector is Peltier cooled (thus it does not require the use of liquid nitrogen) with a cool-down time of less than 2 min. The detector was supplied by the

[1] The inclusion of company names is for completeness and does not represent an endorsement by the National Institute of Standards and Technology.

manufacturer with electronics that include a power supply, cooling control, and four charge-sensitive pre-amplifiers (one for each element). In order to energy-discriminate the pulses from the pre-amplifiers, four Canberra 2026x spectroscopy amplifiers are utilized. The amplifiers have been modified to operate at faster shaping times, down to 0.1 μs, compared with the standard Canberra 2026 amplifiers that operate down to only 0.5 μs. Each filtered output from the shaping amplifiers is fed to its own Ortec 850 quad single-channel analyzer (SCA) for pulse-height energy discrimination. To facilitate cabling, the SCAs have been internally hard wired to receive only one amplifier input per quad unit. Pulse outputs from the SCAs as well as the incoming count rate (ICR) outputs of the Canberra amplifiers are recorded by a National Instruments PXI-1042 crate controlled by *LabVIEW* data acquisition software (Furenlid *et al.*, 1997) that is in wide use at the NSLS for XAFS spectroscopy. In addition, the ICR outputs are directly monitored by four Ortec 449 rate meters. Spectra are acquired by step-scanning a motor (typically either a sample stage or the monochromator) and recording the total number of counts for each output channel of the four detector elements acquired in a specified integration time. Modification for slew scanning would be straight forward. To record the entire energy spectrum, four (one for each detector element) Canberra Multiport II multi-channel analyzers (MCAs) with *Genie* software are utilized. To facilitate setting the SCA windows to detect a particular energy region of interest (ROI), the MCAs are gated by the SCAs. XAFS spectra for a given element are thereby recorded by scanning the monochromator and recording the intensity of a fluorescence line so selected and normalizing to the incidence flux as determined by the current from an I_0 ion chamber upstream of the sample.

3. Results and discussion

Fig. 1 compares an MCA trace from detector element #1 of the SDD with a similar MCA trace from a Canberra single-element SiLi detector with 30 mm^2 active area operating at liquid-nitrogen temperature for the Mn $K\alpha$ and $K\beta$ fluorescence lines (∼6 keV) from a Mn_2O_3 sample. The shaping time of the amplifier was set at 0.1 μs for the SDD and 2 μs for the SiLi detector. Even with the shorter shaping time and larger detector area, the resolution of the SDD exceeds the resolution of the SiLi detector, and it is good enough to resolve the Mn $K\alpha$ and $K\beta$ lines. This energy resolution is therefore sufficient to collect high signal-to-background XAFS spectra in the low-energy X-ray range of a typical high-energy XAFS beamline where overlap between the fluorescence lines and the elastic and Compton scattering peaks of the incident X-ray beam pose the most challenge. The SDD therefore offers a significant improvement (by a factor of approximately ten) in count rate over the smaller area and liquid-nitrogen-cooled SiLi detector.

To characterize the counting efficiency of the SDD, we fabricated an aluminium wedge that was stepped in 2 mm-tall steps each with a depth of 0.25 mm. By step scanning the wedge vertically through the X-ray beam, discrete photon

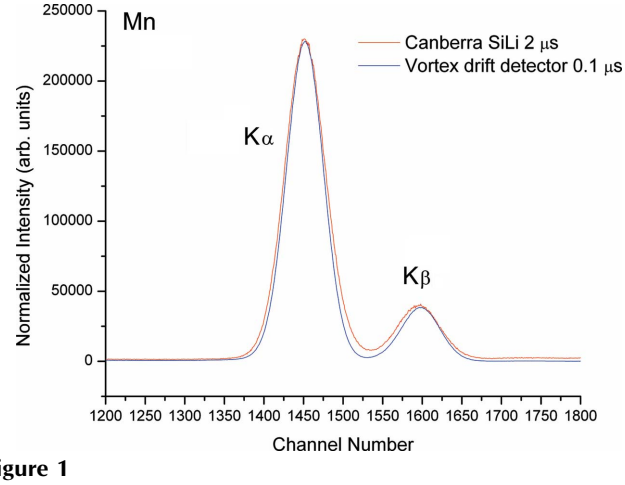

Figure 1
Comparison of an MCA trace for element #1 of the SDD operating at 0.1 μs shaping time with an MCA trace for the single-element SiLi detector operating at 2 μs shaping time for the Mn $K\alpha$ and $K\beta$ fluorescence lines. The curves have been scaled by a constant to make their peak height equal.

fluxes are produced in accordance with Beer's law with no change in beam geometry relative to the four elements of the SDD. The experimental set-up is shown in Fig. 2, along with a picture of the Al wedge. In addition to the SDD that was placed in front of a GeO_2 sample, the set-up consists of an upstream I_{00} ion chamber used in a feedback loop to tune the monochromator, an I_0 ion chamber downstream of the wedge to record the flux incident on the sample, and an I_t ion chamber downstream of the sample to record the flux transmitted through it. The I_t chamber was used to verify the linearity of the I_0 chamber over the full 10^6 dynamic range of the SDD. 'Wedge scans' were recorded at a photon energy of 2.8×10^4 eV to allow transmission of the photon beam through the Al wedge and to minimize the presence of harmonics from the NSLS and the Si(311) monochromator operating at X23A2. All ion chambers were filled with N_2 gas to further insure that the measurements were free of harmonics.

Fig. 3 shows wedge scans for element #1 of the SDD for different shaping-time settings of the Canberra 2026x ampli-

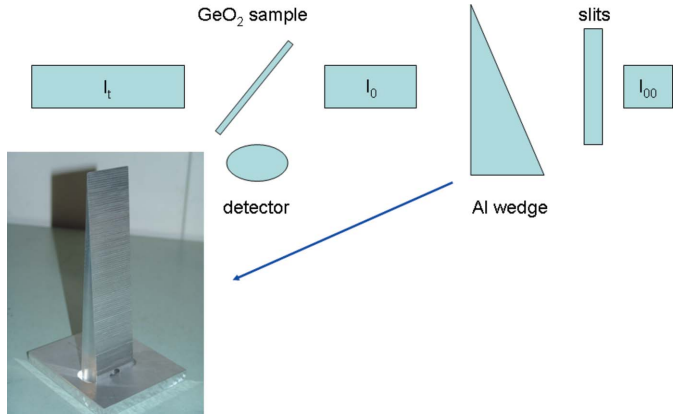

Figure 2
Experimental geometry used to measure detector intensity *versus* I_0 (see text). Also shown is a photograph of the stepped wedge used to vary the photon intensity.

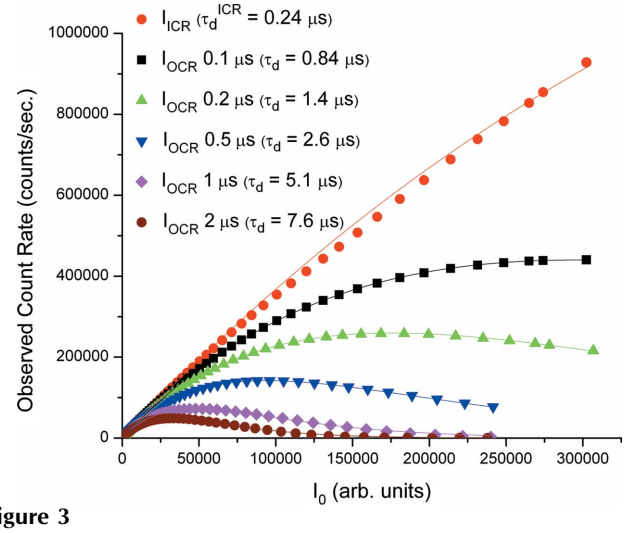

Figure 3
Intensity *versus* I_0 scans measured by scanning the stepped wedge of Fig. 2 vertically through the X-ray beam for element #1 of the SDD as a function of amplifier shaping time. Also shown are the best fits to the data points. The fitted dead-time parameters τ_d are given in the legend (see text).

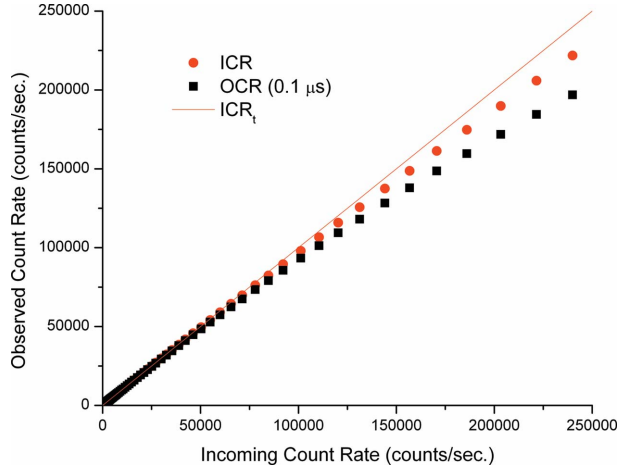

Figure 4
OCR, ICR and ICR_t plotted *versus* ICR_t for low incoming count rate and detector element #1 (see text) operating at 0.1 μs shaping time. Note the non-linearity of the count rate.

fier. The observed count rate (OCR) output that is determined by setting an SCA window from just above the detector/amplifier noise threshold to its upper limit (approximately equal to 60 keV photon energy) is plotted *versus* I_0. Also plotted is the ICR output of the Canberra amplifier itself that has a factory-set shaping- or filter-time constant of 0.043 μs. Note the strong dependence of the maximum attainable count rate (or throughput) on the amplifier shaping time.[2] Assuming Poisson statistics and paralyzable dead-time for a solid-state detector, the OCR output from the SCA should follow the dead-time equation (Knoll, 1989),

$$\mathrm{OCR} = \mathrm{ICR_t} \exp(-\mathrm{ICR_t}\, \tau_d). \quad (1)$$

Here ICR_t is the *true* incoming count rate, and τ_d is the dead-time parameter associated with the SDD element, its pre-amplifier, the Canberra shaping amplifier, and any additional dead-time effects introduced by the pulse-counting electronics. Note that the ICR output will always be less than the true ICR_t count rate owing to its own dead time. Taking the derivative of (1) with respect to ICR_t and setting it equal to zero yields the maximum attainable count rate or throughput for each detector element,

$$\mathrm{OCR_m} = 1/(e\,\tau_d) = 0.37/\tau_d. \quad (2)$$

As we cannot measure ICR_t directly, we assume that it is proportional to I_0: $ICR_t = PI_0$. This assumption allows us to fit the OCR output *versus* I_0 curves of Fig. 3 using only the linear parameter P and the non-linear parameter τ_d for each shaping time,

$$\mathrm{OCR} = PI_0 \exp(-PI_0\tau_d). \quad (3)$$

The results of the fits are plotted in Fig. 3, and the fitted values of τ_d are given in the legend for each amplifier shaping time.[3] Also plotted is a fit to the ICR output of the amplifier itself and its dead-time parameter τ_d^{ICR}.

Despite the roll-off of both the OCR and ICR outputs at high count rate, the response of the OCR and ICR outputs should be linear at low count rates given a fast enough shaping time. Fig. 4 shows OCR, ICR and ICR_t plotted *versus* ICR_t for our fastest shaping time of 0.1 μs. In the plot we have taken $ICR_t = PI_0$. Note that the detector response deviates from linearity by 1% for an incoming count rate of 1.2×10^4 counts per second per detector element, and this non-linearity grows to 10% for an incoming count rate of 1.25×10^5 counts per second per detector element. Consequently, although the detector is capable of energy-discriminating photons in excess of 4×10^5 counts per second per detector element ($OCR_m = 4.38 \times 10^5$ counts per second per detector element for shaping time equal to 0.1 μs), in order to record accurate XAFS spectra it appears necessary to apply a dead-time correction for count rates as low as 1×10^4 counts per second per detector element.

To correct XAFS spectra for dead-time, we follow the suggestions given by Cramer *et al.* (1988), Nomura (1998), Ciatto *et al.* (2004*a*,*b*) and Warburton (2004). As discussed, in addition to collecting the energy-discriminated fluorescence ROI for each detector element, it is also necessary to record both the OCR and ICR outputs for each detector element.

Because the entire energy spectrum of an OCR output is affected uniformly by dead-time,[4] the dead-time-corrected ROI_{corr} count rate for each element may be approximated by

[2] We also tested the performance of the detector with digital XIA electronics. The maximum throughput of the detector when operating with digital electronics was within 10% of the maximum throughput when operating with analog electronics for similar energy resolution.

[3] P depends strongly on the experimental conditions (photon energy, detector/sample geometry, gain, length, and gas of ion chamber *etc.*), whereas τ_d should depend only on the amplifier shaping time. For the data plotted in Figs. 3, 4 and 7, P was equal to 4.05. Note that it should be verified that the P values are equal for the OCR and ICR channels.

[4] We verified this experimentally by placing a Mn_2O_3 sample in front of the GeO_2 sample of Fig. 2 and recording wedge scans. ROIs set to monitor the Mn $K\alpha$ and Ge $K\alpha$ fluorescence lines as well as the OCR output differed by only constant scale factors for each element over the entire photon intensity range.

$$\mathrm{ROI_{corr}} = \mathrm{ROI} \times \mathrm{ICR_t}/\mathrm{OCR}. \quad (4)$$

As emphasized by Warburton (2004), it is necessary to use the true incoming count rate $\mathrm{ICR_t}$ in (4) because the ICR itself also suffers from dead-time loss. This is especially true when the shaping time of the amplifier is close to the shaping or filter-response time of the ICR channel, as is the case for our SDD. Each $\mathrm{ICR_t}$ then is obtained by measuring $\tau_\mathrm{d}^\mathrm{ICR}$ as in Figs. 2 and 3 for each detector element and numerically inverting,

$$\mathrm{ICR} = \mathrm{ICR_t} \exp\left(-\mathrm{ICR_t}\, \tau_\mathrm{d}^\mathrm{ICR}\right). \quad (5)$$

This inversion is evaluated point-by-point and for each detector element using an iterative algorithm, expressed here in pseudocode:

```
// without a known dead time, do a simple ICR/OCR
correction //
if (DeadTime = 0); do:
CorrectedROI := ROI * ICR / OCR
return
end if
// given a value for dead time, iteratively correct
the ICR //
Test := 10**8
TestICR := ICR
while (Test > DeadTime); do:
TrueICR := ICR * exp(TestICR * DeadTime)
Test := (TrueICR - TestICR) / TestICR
TestICR := TrueICR
end while
CorrectedROI := ROI * TrueICR / OCR
return
```

Care must be taken to normalize the measured ICR and OCR by the integration time, to terminate the loop if it fails to converge in a reasonable number of steps [as the loop will not terminate if OCR is greater than the $\mathrm{OCR_m}$ value defined in (2)], and not to perform the iteration if the measured ICR is zero or less (as might happen in the event of a beam dump).

This dead-time correction scheme has been incorporated into the *ATHENA* XAFS data analysis program (Ravel & Newville, 2005). Given a data file containing the three data channels for each detector element (ROI, OCR, and ICR) together with the total integration time and I_0 intensity as a function of photon energy, knowledge of $\tau_\mathrm{d}^\mathrm{ICR}$ for each detector element allows *ATHENA* to transparently produce corrected XAFS spectra. When $\tau_\mathrm{d}^\mathrm{ICR}$ is not known, inputting a value of zero for $\tau_\mathrm{d}^\mathrm{ICR}$ into *ATHENA* simplifies the correction to

$$\mathrm{ROI_{corr}} = \mathrm{ROI} \times \mathrm{ICR}/\mathrm{OCR}, \quad (6)$$

i.e., it is assumed that the ICR channel does not suffer dead-time loss. For slower SiLi or GeLi detectors that require longer shaping times than the SDD, this may be an adequate approximation.

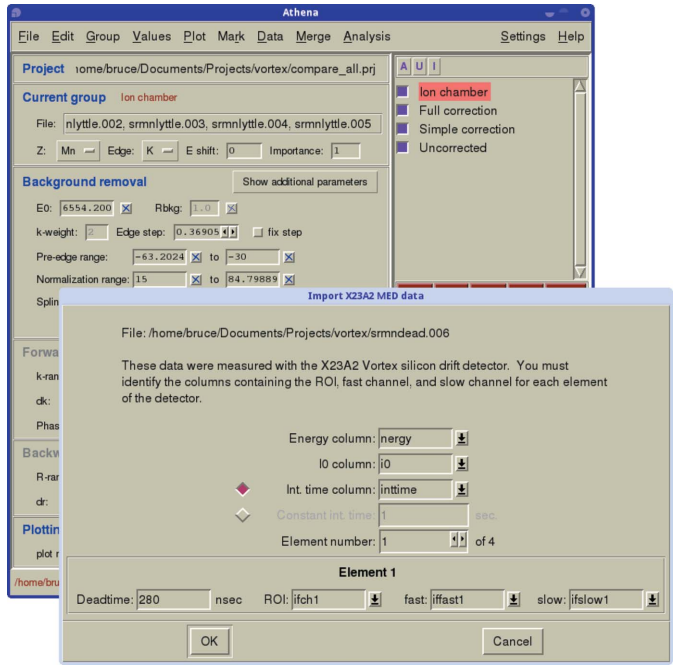

Figure 5
ATHENA dead-time dialogue window implemented to correct XAFS spectra for dead-time. The dialogue may be modified for an arbitrary number of channels.

To demonstrate the dead-time correction as implemented in *ATHENA*, Fig. 5 shows the *ATHENA* dead-time dialogue window, and Fig. 6 shows Mn *K*-edge XAFS spectra from $SrMnO_3$ recorded with an ICR count rate of approximately 7×10^5 counts per second per detector element at 0.1 µs shaping time. At this count rate the detector is operating close to its maximum throughput, $\mathrm{OCR_m}$. Clearly, dead-time correction of both the ROI and ICR outputs is necessary. Once the total correction has been made, data from the SDD and an ion chamber (Stern & Heald, 1979) that do not suffer from dead-time loss are indistinguishable.

As a final note, although the algorithm is capable of correcting XAFS spectra at count rates approximating the maximum throughput of each detector element, as seen from Fig. 3, at the maximum throughput the collection efficiency of the detector is equal to zero; *i.e.*, $\mathrm{d(OCR)/d(ICR_t)} = 0$, and the detector is no longer able to energy-discriminate photons. The detector therefore performs not as an energy-discriminating detector but rather as a total fluorescence-yield detector through the faster amplifier ICR outputs. This situation will lead to XAFS spectra with significantly reduced signal-to-background ratios and inferior performance compared with an ion chamber (Stern & Heald, 1979). To avoid such inefficient use of the detector, we suggest that the true incoming count rate should not exceed the maximum throughput of the detector,

$$\mathrm{ICR_t} \leq \mathrm{OCR_m} = 1/(e\,\tau_\mathrm{d}). \quad (7)$$

It can then be shown that $\mathrm{d(OCR)/d(ICR_t)} \geq 0.44$, and the detector therefore will be operating near to or better than

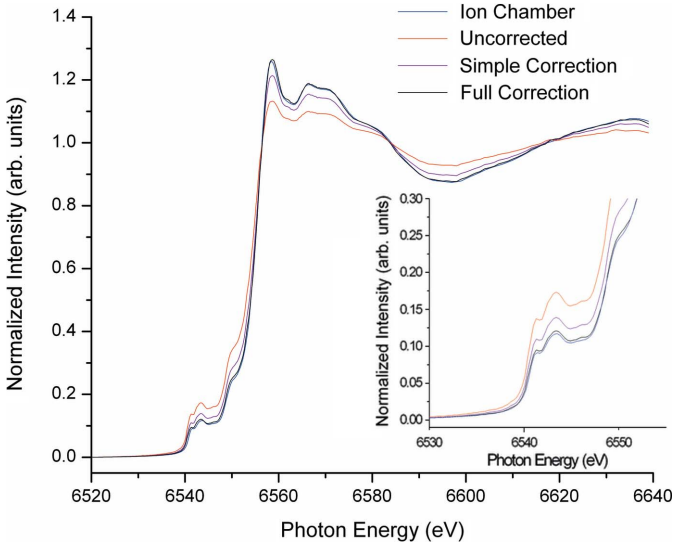

Figure 6
Illustration of the *ATHENA* XAFS dead-time correction. Shown is the SDD spectrum from $SrMnO_3$ uncorrected for dead-time, the SDD spectrum corrected for dead-time assuming $\tau_d^{ICR} = 0$ (simple correction), and the SDD spectrum corrected for dead-time using the experimentally determined values for τ_d^{ICR} (full correction). The SDD spectra are compared with the spectrum acquired by an ion chamber that suffers no dead-time loss. Note that in the latter case the two spectra are indistinguishable. The inset shows an expanded view of the Mn pre-edge feature.

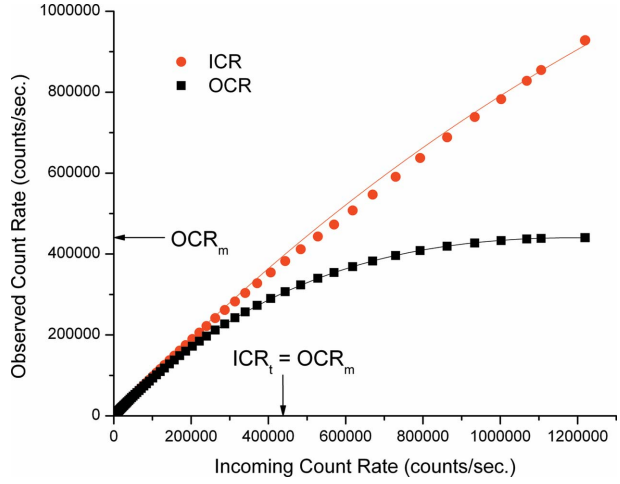

Figure 7
OCR and ICR *versus* ICR_t for detector element #1. Shown is our suggested maximum count rate, *i.e.*, $ICR_t \leq OCR_m$ (see text). Note that when $ICR_t = OCR_m$, the detector is operating close to 50% of its maximum counting efficiency.

50% of its maximum collection efficiency. At this count rate, $OCR = 0.69 OCR_m$, and a relatively high count rate (3×10^5 counts per second per detector element or 1.2×10^6 total counts per second for all four elements summed) for our SDD operating at 0.1 μs shaping time is still preserved. Note that the value of τ_d^{ICR} should be determined from a fit of the ICR *versus* I_0 data that are also limited to this maximum counting rate, because the extreme high-count-rate performance of the detector may be affected by the timing structure of the synchrotron (Walko *et al.*, 2008). When the detector is operated at count rates exceeding 70% of its maximum throughput, then the extent of photon pile-up will depend on the details of the fill pattern, and the dead-time parameter τ_d should be determined independently for each timing structure. Fig. 7 shows a graph of the OCR and ICR outputs for detector element #1 plotted *versus* ICR_t along with our maximum suggested incoming count rate OCR_m.

4. Conclusion

We have described the performance of a four-element SDD operating at the NIST beamline X23A2 at the NSLS. The detector is capable of acquiring accurate high signal-to-background dead-time-corrected EXAFS spectra at count rates exceeding 1.2×10^6 counts per second for all four channels summed. The dead-time algorithm has been implemented into the *ATHENA* data analysis software that should benefit the EXAFS community.

The authors thank Pavel Rehak for useful discussions and Igor Levin for the $SrMnO_3$ sample. Data were collected at the National Synchrotron Light Source. Use of the National Synchrotron Light Source, Brookhaven National Laboratory, was supported by the US Department of Energy, Office of Science, Office of Basic Energy Sciences, under Contract No. DE-AC02-98CH10886. Additional support was provided by the National Institute of Standards and Technology.

References

Ciatto, G., d'Acapito, F., Boscherini, F. & Mobilio, S. (2004). *J. Synchrotron Rad.* **11**, 278–283.
Ciatto, G., d'Acapito, F., Boscherini, F. & Mobilio, S. (2004). *J. Synchrotron Rad.* **11**, 509.
Cramer, S. P., Tench, O., Yocum, M. & George, G. N. (1988). *Nucl. Instrum. Methods Phys. Res. A*, **266**, 586–591.
Furenlid, L. R., Mayer, A. J. & Kirkland, J. P. (1997). *J. Phys. IV*, **7**, C2-335–C2-336.
Gatti, E. & Rehak, P. (1984). *Nucl. Instrum. Methods Phys. Res.* **225**, 608–614.
Knoll, G. F. (1989). *Radiation Detection and Measurement*, ch. 4. New York: Wiley.
Letard, I., Tucoulou, R., Bleuet, P., Martinez-Criado, G., Somogyi, A., Vince, L., Morse, J. & Susini, J. (2006). *Rev. Sci. Instrum.* **77**, 063705.
Nomura, M. (1998). *J. Synchrotron Rad.* **5**, 851–853.
Ravel, B. & Newville, M. (2005). *J. Synchrotron Rad.* **12**, 537–541.
Stern, E. A. & Heald, S. M. (1979). *Rev. Sci. Instrum.* **50**, 1579.
Strüder, L., Lechner, P. & Leutenegger, P. (1998). *Naturwissenschaften*, **85**, 539–543.
Walko, D. A., Arms, D. A. & Landahl, E. C. (2008). *J. Synchrotron Rad.* **15**, 612–617.
Warburton, W. K. (2004). *J. Synchrotron Rad.* **11**, 508.
Welter, E., Hansen, K., Reckleben, C. & Diehl, I. (2009). *J. Synchrotron Rad.* **16**, 293–298.